

Article

# Synthesis of SiC/BiOCl Composites and Its Efficient Photocatalytic Activity

Wanli Liu, Qi Li, Xianglong Yang \*, Xiufang Chen \* and Xiangang Xu

State Key Laboratory of Crystal Materials, Shandong University, Jinan 250100, China;

lwlsdu@mail.sdu.edu.cn (W.L.); liqi1995@mail.sdu.edu.cn (Q.L.); xxu@sdu.edu.cn (X.X.)

\* Correspondence: yangxl2016@sdu.edu.cn (X.Y.); cxf@sdu.edu.cn (X.C.); Tel.: +86-531-88366329 (X.Y. &amp; X.C.)

Received: 21 July 2020; Accepted: 9 August 2020; Published: 18 August 2020



**Abstract:** BiOCl nanosheets nucleated and grew on cottage cheese-like SiC substrate via hydrothermal procedure, through which a tight heterojunction was formed. SiC/BiOCl composites with varied morphologies were acquired that the formation of BiOCl was involved with different form of carbon existed on surface of SiC. The photocatalytic mechanism analysis revealed that the combination of SiC and BOC significantly enhanced photocatalytic activities owing to the improved visible light utilization, efficient separation of photo-generated carriers, and promoted reactive area. The main active species during the photocatalytic reaction was determined as  $\cdot\text{O}^{2-}$  radical by additionally adding trapping agent into the reactant. The SiC-BOC composites showed much higher photoactivities in photocurrent responses and photocatalytic degradation of TC-HCl, which mainly attributed to the well-built heterointerface promoted by Bi-C bonds and the interlaced structure obtained by increasing exposure of (010) facets in BiOCl. The nucleation, growth and combination architecture of BiOCl was all influenced by the involvement of SiC.

**Keywords:** SiC; BiOCl; photocatalysis; degradation of TC-HCl; hydrogen production

## 1. Instruction

Nowadays, with the scarcity of water resources, water pollution became a critical problem to be resolved, and is mainly caused by various organic pollutants such as antibiotics and dye [1]. Pharmaceuticals, as the emerging pollutants in water system, would act on the water quality and water supplies, and may constitute a potential risk for the ecosystems in the long term. Photocatalytic degradation of organic pollutant based on the sustainable solar light acting as driving force became a promising technique for solving these environmental issues. Bismuth oxychloride (BiOCl), as a novel ternary oxide semiconductor, has drawn considerable research attention for its open crystalline structure and unique layered architecture. The tetragonal layered structure of BiOCl were composed of alternating double  $\text{Cl}^-$  slice and  $[\text{Bi}_2\text{O}_2]$  layers that stacked through the nonbonding interaction of Cl atoms in the [001] direction [2] as shown in Figure 1, whose space between the layers is enough to polarize the proximal atoms and orbitals, and induce the formation of internal static electric fields (IEF) perpendicular to the slabs, thus exhibiting distinguished potential properties in the photocatalysis field [3,4]. Until now, many strategies have been studied on how BiOCl worked as photocatalyst, including morphologies [5], crystal facet exposure [6,7], self-doping [8], defect [9] and surface complex [10–12]. However, the deficient optical properties, limited absorption capacity and recombination of photo-induced electrons and holes also restricted the development of BiOCl. Fabricating a heterojunction [13] was proved to be a valid and widely used method for BiOCl to overcome the disadvantage for photocatalytic activity by well-built combination between two semiconductors.

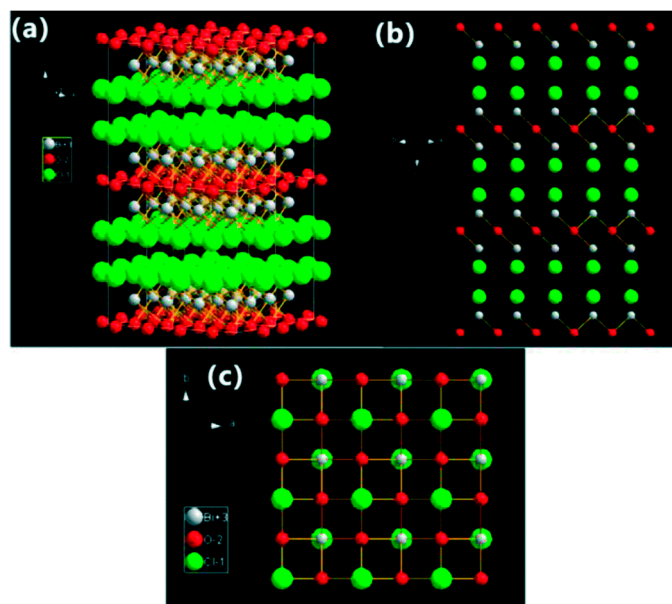


**Figure 1.** Layered structure model illustrations of BiOCl: (a) three-dimensional spatial structure, (b) {110} facets and (c) {001} facets. Reproduced with permission from [14]. Copyright 2014, The Royal Society of Chemistry.

SiC, as a carbon-based semiconductor with tunable band gap (2.3–3.3 eV) [15], performed excellent chemical stability and high carrier mobility which was also green, non-toxic and rich in raw materials [16]. As we know, thermal decomposition on the surface of SiC would reorder the carbon wrapped on it which resulted a core–shell-like heterojunction structure and incorporated the advantage of carbon such as high conductivity and adsorption [17,18]. By adjusting the synthesis process or high-temperature graphitization, different contents and forms of carbon on the surface of SiC can be realized naturally which could further affect the formation of other materials during the compound, while the morphology of BiOCl attached closely to the growth of the (010) facet which was sensitive to the solvent used in the synthesis process [19]. Organic solvents, ionic liquids (ILs) and surfactants had been applied to tailor the morphology of BiOX [20] to obtain a high activity of the catalyst.

In this paper, a series of SiC/BiOCl (SiC/BOC) photocatalyst composites were prepared through hydrothermal method with different types of SiC. The obtained BOC plate adhered on the surface of microporous SiC, where the heterojunction structure was successfully constructed. Furthermore, the carbon wrapped on SiC played a key role in the growth of BiOCl and, even more, influenced the photoactivity. The results showed that the SiC-BOC photocatalyst had a remarkably enhanced TC-HCl photodegradation activity under solar light irradiation comparing with pure SiC and BiOCl. How did the carbon-coated SiC influence the evolution of BiOCl and combination architecture between those two was detailed discussed in this paper. The photocatalytic mechanism of SiC-BOC composites was also investigated on the basis of the experimental and relative band positions of these two semiconductors.

## 2. Results and Discussion

### *Synthesis and Characterization*

The X-ray diffraction (XRD) patterns of the pure BiOCl, SiC-BOC, SiC-G-BOC and SiC-C-BOC heterojunction photocatalysts were shown in Figure 2a. The diffraction peaks of BiOCl nanosheets indexed as tetragonal-phase BiOCl (by reference to JCPDS no. 06-0249) appeared in all the composites, implying the perfect formation of BiOCl. The small peak at 35° was due to cubic SiC (ICSD PDF: 29-1129). Owing to the concentrated cover of BOC nanosheet on the SiC surface and a relatively low diffraction intensity, the peak of SiC was not obvious. With the variation from SiC-BOC to SiC-C-BOC, the values of the  $I(001)/I(110)$  in the composite increased from 0.43 to 0.49 relevantly, as displayed in

Table 1. Consequently, the intensity of (001) peak in SiC-C-BOC became sharper and stronger with the decrease of (110), which notified the preferred growth along the [001] orientations leading to the heavier thickness [21]. By contrast, as the intensity of (010) characteristic peak increased, the growth along the [001] direction was weakened, leading to a thinner thickness and lessened areas [21] which comes to the formation of tiny sheet-like building units. Calculated by software Jade 5.0 based on Scherer formula, the thicknesses (along (001) direction) of SiC-BOC, SiC-G-BOC and SiC-C-BOC were measured to be 32.1, 53.5 and 101.6 nm, as well as the width (along (110) plane) to be 133.5, 171.0 and 198.6 nm, respectively. In summary, the BOC samples prepared with specific SiC exhibited distinct differences of shape in plane size and thickness. After high-temperature graphitization, the carbon on the surface was reordered and grew in number as a result of the loss of Si by evaporation. However, the crystallization of BOC in SiC-G-BOC was not weakened by the increasing concentration of carbon compared with SiC-BOC. That is to say the form of carbon played a decisive role on the growth of BiOCl on SiC rather than the contents. The XRD pattern ( $11^{\circ}$ – $12^{\circ}$ ) of SiC-BOC composites in Figure 2b showed that the half width of (001) peak varied but not lined with the increase of carbon, which also supported the view. This result was in agreement with FESEM data behind and also can support the difference of the thicknesses discussed above.

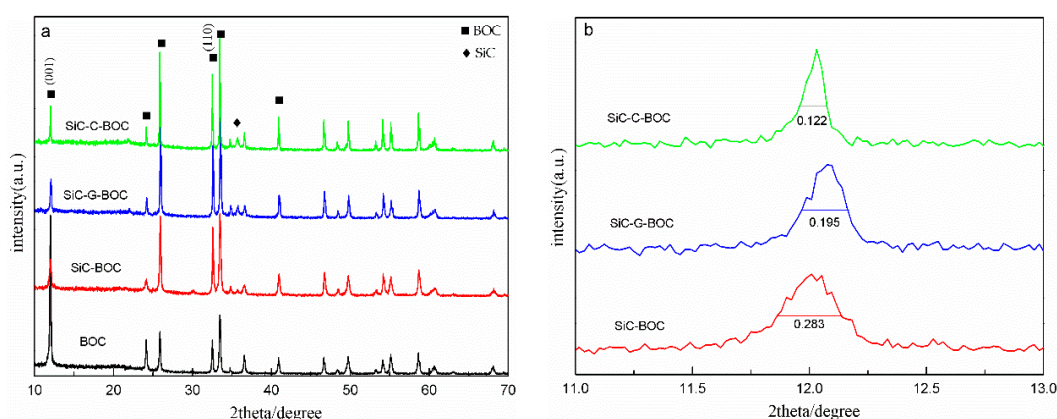


**Figure 2.** X-ray diffraction (XRD) patterns of BOC, SiC-BOC, SiC-G-BOC and SiC-C-BOC (a) and the magnification of the diffraction peak (001) (b).

**Table 1.** Specific value of (110) and (001) peak and the FWHM of (001) and (110) characteristic peak.

	I(001)/I(110)	FWHM (001)
SiC-BOC	0.43	2.83
SiC-G-BOC	0.46	1.95
SiC-C-BOC	0.49	1.22
BOC	8.30	-

X-ray photoelectron spectroscopy measurement was employed to determine chemical state and surface properties of the catalysts. Figure 3a showed the full XPS spectrum of SiC-BOC and SiC-G-BOC from which the peak of Bi, O, Cl, Si and C elements could be identified. The component of C1s at the lowest binding energy 283.4 eV in Figure 3c corresponded to the C-Si bonds [22]. The peak around 284.5 eV was attributed to graphite carbon or contaminant carbon. The C1s peaks at 285.6 and 288.1 eV were assigned to the C–O and C=O oxygen-containing carbonaceous bands [23]. Moreover, an additional shoulder-peak located at 281.7 eV was found only in SiC-BOC which evidenced the presence of Bi-C [24]. The formation of the Bi–C bond also can be confirmed by analysis of the Bi (4f) core level of the XPS spectra, as shown in Figure 3d,e. Bi-binding energies at 160.3 and 165.4 eV were allocated to the Bi (4f<sub>5/2</sub>) and Bi (4f<sub>7/2</sub>) of Bi<sup>3+</sup> [25], respectively, as well as the 5.3 eV gap between them confirming the normal chemical state of BiOCl. The extra two peaks with lower binding energy at approximately 163.6 and 158.4 eV (relating to the Bi 4f<sub>5/2</sub> and 4f<sub>7/2</sub> peaks) probably arose out of a

Bi–C bond between SiC and BOC, since the binding energy was lower than that of Bi–O and Bi–Cl bonds [26]. By contrast, the rising area ratio of those two lower peaks further indicated the stronger contact by Bi–C in SiC-BOC. The O 1s core level spectrum of BOC can be deconvoluted into three peaks [27], the peaks positioned at 529.7 and 532.4 eV were attributed to O–Bi ( $O_L$ ) in the BOC lattice and loosely chemisorbed oxygen on the surface of BiOCl, respectively. Moreover, the medium peak centered at 531.7 eV in Figure 3f was assigned to  $O^{2-}$  ( $O_V$ ) which existed in the oxygen deficient area, clearly revealing the presence and increment of oxygen vacancies in SiC-BOC. The area ratio of  $O^{2-}$ -BOC to O-BOC ( $A(O_V/O_L)$ ) offered a helpful method to evaluate the concentration of oxygen vacancy [27]. The calculated values of  $A(O_V/O_L)$  for SiC-BOC was 1.37, as well as for SiC-G-BOC was 1.06. The enlarged amount of oxygen vacancies in SiC-BOC can be demonstrated by its higher calculated values. A slight shift towards lower binding energies was observed in C 1s, Bi 4f and O 1s peaks of SiC-BOC compared to SiC-G-BOC, implying a tighter interfacial contact. The XPS spectra disclosed the existence of Bi–C chemical bonds between SiC and BiOCl, and the interaction in SiC-BOC was stronger than that in SiC-G-BOC composites. More oxygen vacancies were also achieved in SiC-BOC verified by the increasing area ratio of characteristic peaks, which may come from the higher reactive facet exposure and polar percentages.

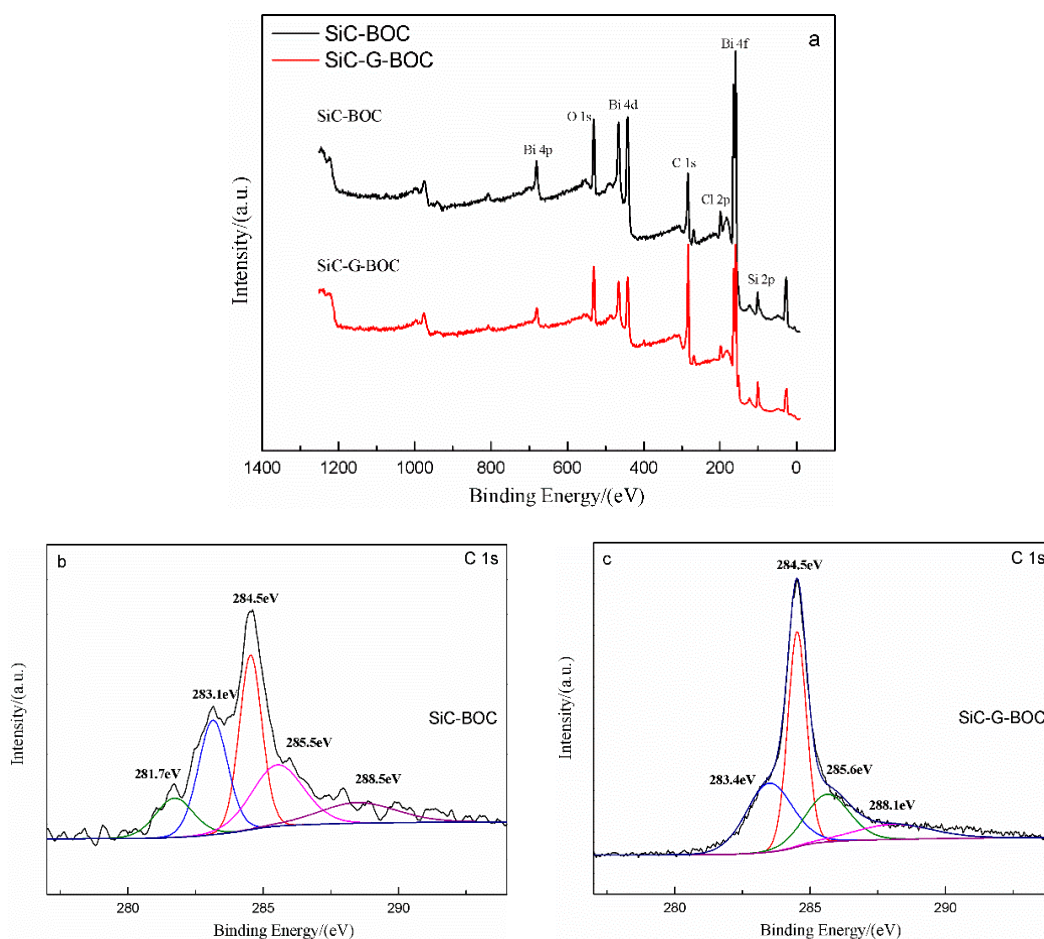
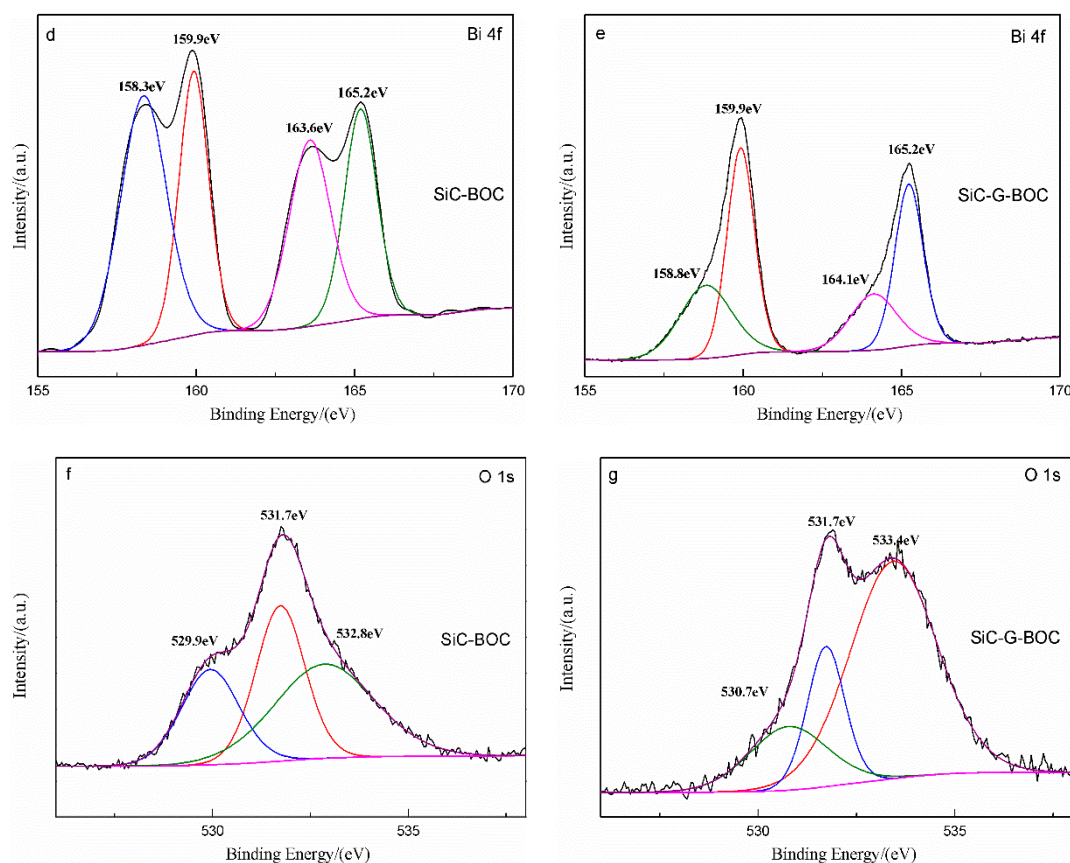


Figure 3. Cont.



**Figure 3.** The XPS spectra of (a) survey (b,c) C 1 s, (d–f) Bi 4f and (f,g) O 1 s.

The SEM results showed the morphology of the composite, with BOC nanosheets nucleated and aggregated on the surface of SiC, partially adhering to the rough surface of the cottage cheese-like bulk SiC. The high magnification image revealed the characteristics of pure SiC and BOC, and the contact way between them two. In order to tell the distinction of the composites, the morphology variation and distribution difference was presented on the right side. The pore characteristics and roughness of SiC bulk was relevantly changeable depending on the size of the constituent units. SiC-C bulk was composed by the largest particles with obvious gaps, due to the regrowth and burn of the carbon coated on it. Comparatively, the surface of SiC bulk displayed in Figure 4e was sponge-like and rich in tiny holes, which attributed to its trifling granularity and carbon filling. Contrast with SiC-BOC, SiC-G-BOC presented expanded size of units and pores after reorder of carbon and recrystallization of SiC [28]. It is noticeable that BOC nanosheets also displayed extremely dissimilar appearance on respective SiC bulk. The BOC in SiC-C-BOC illustrated disk-like structures that were so large they hardly overlapped on the surface of irregular cottage cheese-like SiC, leading to a rare contact. For SiC-G-BOC, the formed BOC of square posted on the surface of SiC-G bulk owing to the significant diminished size. The shape of BOC in SiC-BOC was smaller and thinner, with which filled the interspace in SiC bulk and formed more sufficient contact, as shown in Figure 4e,f. Additionally, it seemed that the tiny slab of BOC in SiC-BOC tended to aggregate self-assembly into feathery-like structure to reduce the surface energy, rather than the layer-stacked structure in SiC-G-BOC. For the carbon-coated SiC, amorphous carbon remaining on its surface was dispersed into the water like surfactant, so that the young nuclei were not easy to reunite together during the process and inhibited the growth along [001] direction, resulting in the final building block with small dimension [29,30]. During the formation of the SiC-BOC hybrid, SiC not only provided a facile substrate for the nucleation and subsequent growth of BOC, but also mediated the morphologies of BOC. That is to say, the shape of SiC and the connection between carbon and SiC was the main reason for the difference of the composites. Therefore, the resulted BOC

nanosheets with appropriate size can amply deposit on SiC bulk and stick to its rough surface, leading to the construction of more effective heterojunction interfaces by enlarging contact area, and providing a potential advantage for the enhancement of charge separation. With the increasing exposure of (010) facets, the mixed structure with interlaced nanosheets can enhance the adsorption and reaction activity by greatly increasing the surface areas of the photocatalyst and, thus, for the improvement of photocatalytic performance [31].

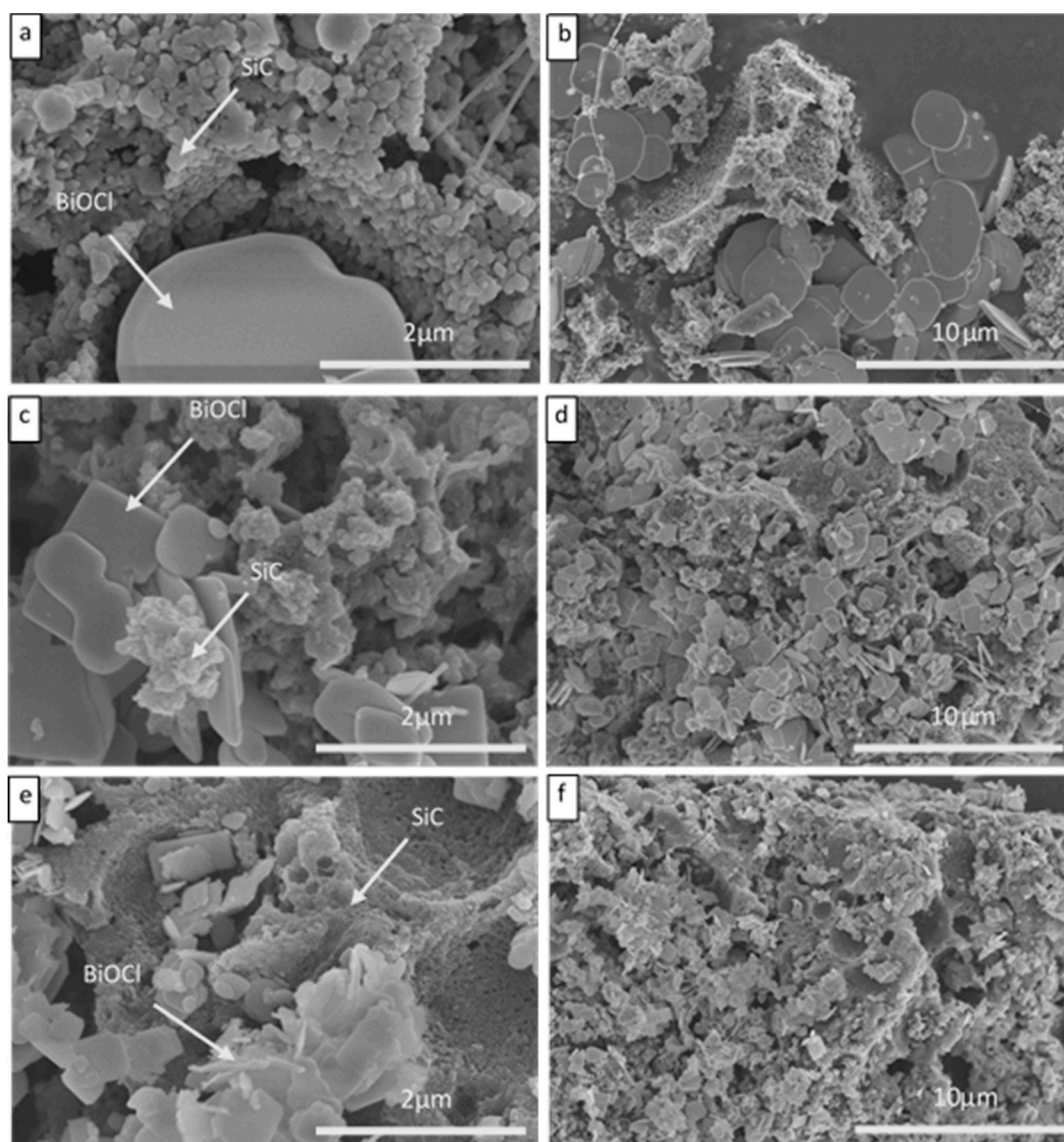


**Figure 4.** SEM images of (a,b) SiC-C-BOC, (c,d) SiC-G-BOC and (e,f) SiC-BOC.

To provide further insights into the morphology and structure of the composite materials, high-resolution photographs were taken by transmission electron microscopy (TEM). The low magnification TEM image in Figure 5a clearly showed that morphology of SiC-C-BOC was composed by square-shaped plate of BiOCl and Irregular structure of SiC, while the other two sample displayed a mixed structure without significant characteristics of the two components. More details about the crystal structure and morphology of as-prepared samples were obtained from the high-resolution TEM (HRTEM) image as shown in Figure 5b,d,f. The clear lattice fringes with an interplanar lattice spacing of 0.275 nm observed in each sample was corresponded to the (110) atomic planes, by which the top and bottom surface of BOC nanosheets was identified as (001) facets [32]. Furthermore, the well-defined lattice fringe interval with  $d = 0.25$  nm which corresponded to the (111) facet of SiC crystals were

also found on continuous lattice fringes of BOC-(110), indicating that tight coupling between BOC and SiC happened on BOC-(001) facets and SiC-(111) facets [33]. Combined with the SEM results, the formation of SiC-BiOCl heterojunction was verified by the smooth interface. Moreover, another three kinds of lattice fringes with  $d$  spacing of about 0.738, 0.386, and 0.335 nm were observed by HRTEM in SiC-BOC (Figure 5f), which can be indexed as the (001) and (002) planes of BiOCl, and the (004) plane of Carbon, respectively. The diverse orientations and criss-cross of lattice fringe existed in SiC-BOC demonstrated the staggered structure, and this illustrated the feathery-like architecture resulting from the increasing exposure of (010) facets, which was in agreement with the SEM and XRD results. Even though the growth of BOC-001 was constrained by the influence of SiC, (001) facets were still the preferentially exposed facets whose abundant oxygen vacancies can enhance the separation efficiency of electron-hole pairs.

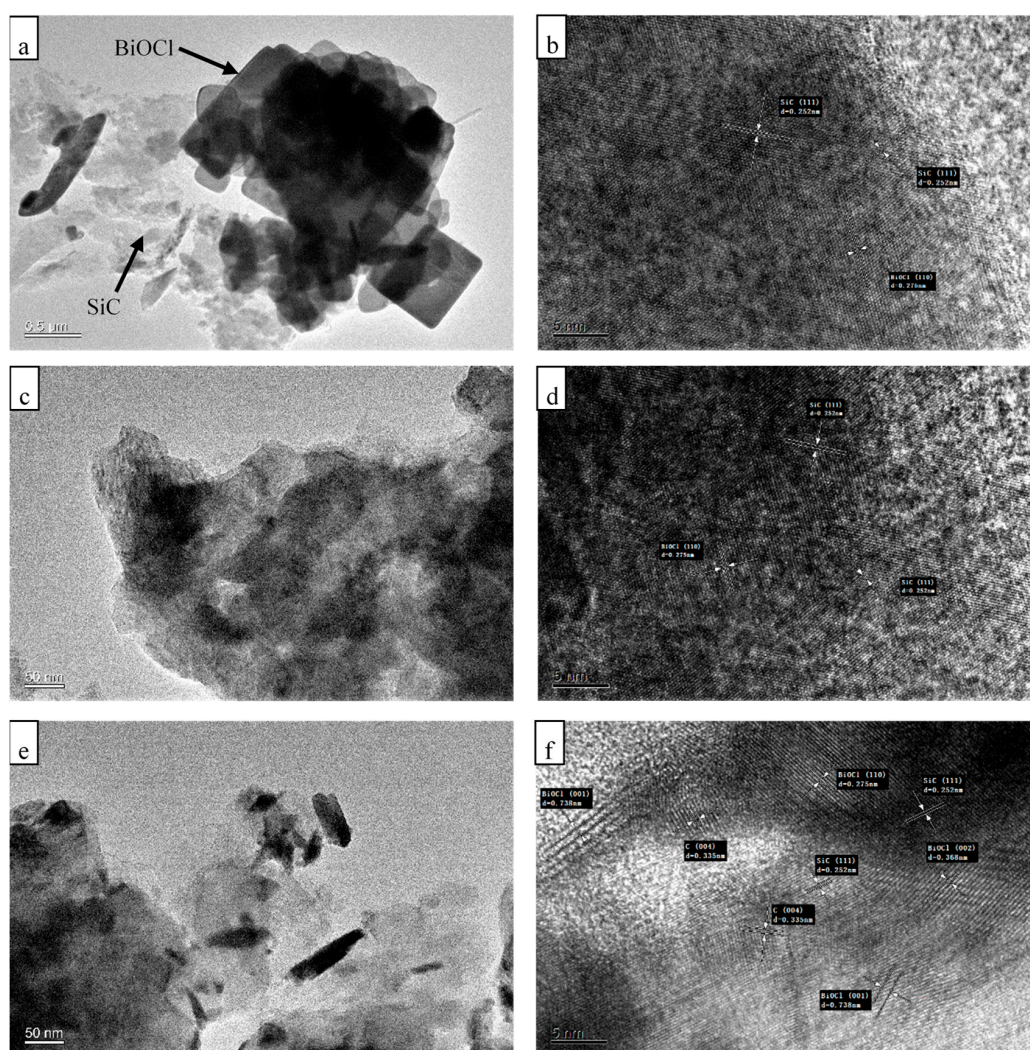


**Figure 5.** TEM and HR-TEM images of (a,b) SiC-C-BOC, (c,d) SiC-G-BOC and (e,f) SiC-BOC.

The thermal properties and the composition of the raw materials SiC and SiC/BOC hybrids were characterized by thermogravimetric (TG) analysis as displayed in Figure 6, which was performed in air atmosphere with a heating rate of 10 °C/min. The result of SiC samples pointed out an easier loss of carbon in SiC-BOC, as well as higher quantities of carbon in SiC-G-BOC coming from the evaporation of Si during the high-temperature graphitization. The significant decline from 555 to 675 °C was shown in the curves of carbon-coated SiC, which was attributed to the removal of carbon, announcing the amount of carbon was 43.9% in SiC and 47.5% in SiC-G. For the composite, the slight weight loss before

100 °C was attributed to the evaporation of water and ethanol adsorbed on the surface. A gradual mass loss was observed with climbing temperature to 450 °C, which was associated with the burning of carbon layers. When the temperature rose to 720 °C, the samples exhibited another remarkable weight loss on account of the conversion from BiOCl to Bi<sub>2</sub>O<sub>3</sub> and BiCl<sub>3</sub> [34]. Compared with SiC-G-BOC, a promoted thermal stability was achieved in SiC-BOC owing to the chemical coupling through Bi-C bonds and tight effective contact.

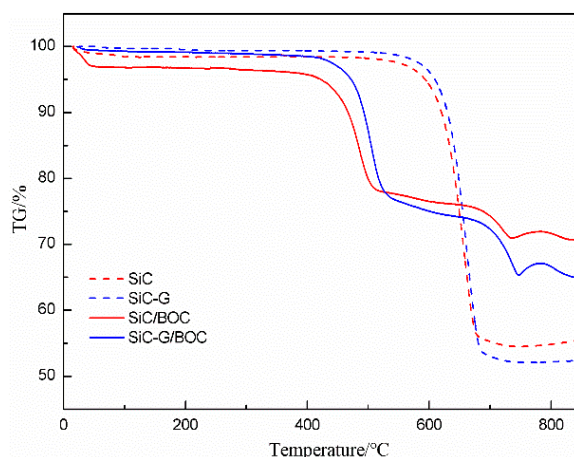


Figure 6. TG curves of SiC and SiC/BOC composites.

The Brunauer–Emmett–Teller (BET)-specific surface areas of the as-prepared samples were investigated by nitrogen adsorption measurements. Based on IUPAC classification [35], the isotherm of SiC-BOC and SiC-G-BOC revealed that the microporous adsorption mainly benefited from that carbon filled up the narrowed gap between the tiny SiC particles. By contrast, SiC-C-BOC showed a totally distinct type of curve aroused from the intra-aggregation of plate-like BOC crystals, but similar with pure BOC as shown in Figure 7b. These results were consistent with  $S_{BET}$  results and SEM observation. The BET-specific surface area of SiC-BOC was calculated to be 197 m<sup>2</sup>/g, whereas pure BOC exhibited a BET area of 5.3 m<sup>2</sup>/g. The expanded specific surface area after combination of SiC and BOC remarkably enlarged the reactive area, which favored the increase in number of heterojunction interfaces. The microporosity from carbon-coated SiC not only assisted the transport towards reactants by promoted adsorption capacity, but also enhanced light utilization owing to the multiple reflections within the interior cavity. The slight improvement in SiC-BOC ( $S_{BET} = 197$  m<sup>2</sup>/g) compared with SiC-G-BOC ( $S_{BET} = 177$  m<sup>2</sup>/g) was owing to the tiny and interlaced structure by increasing exposure of (010) facets which offered more active sites and open space to further lift the adsorption efficiency and reaction rate.

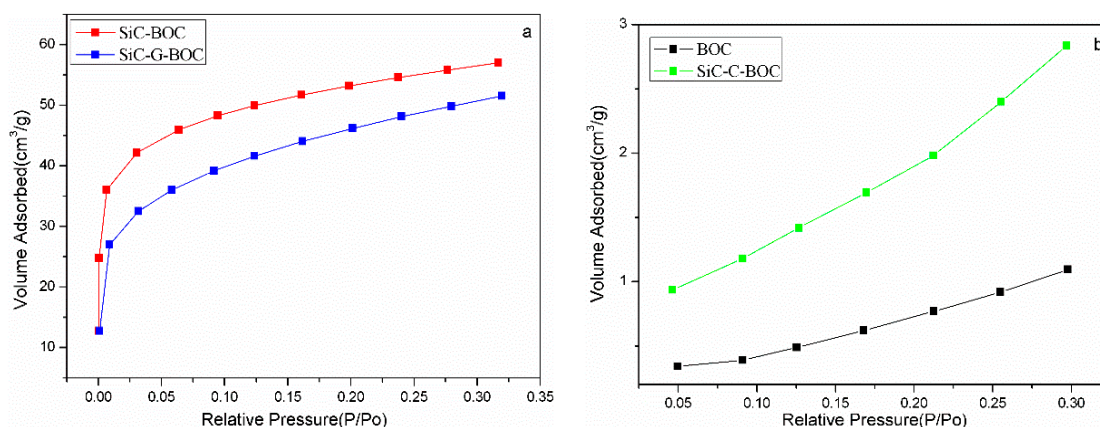


Figure 7. Nitrogen adsorption isotherm of (a) SiC-BOC, SiC-G-BOC and (b) BiOCl, SiC-C-BOC.

UV-vis diffuse reflectance spectrometer (DRS) was used to judge the photoabsorption ability and band gap energy of the synthesized samples. As evident in Figure 8, pure BOC with an absorption edge of approximately 375 nm and negligible absorption in the visible region. However, all investigated SiC/BOC hybrids exhibited a notable enhancement of absorption in the whole range and a red shift of absorption edge resulted from the introduction of SiC, which functioned as a light sensitizer in the heterojunctions. The narrowing band gap signified an improving utilization of sunlight. Compared to SiC-G-BOC, SiC-BOC displayed decreased absorption in UV but better visible light harvest above 800 nm and red-shift of adsorption edge, indicating that sunlight-driven photocatalytic activities were improved and the concentration of oxygen vacancies raised. Those advantages were attributed to the specific morphology and band structure of SiC-BOC. On one hand, the thickness of BiOCl reduced with the growth of (010) activity facets, which resulted in the change of the predominant defect on the surface of BOC from  $V_{Bi}'''$  to  $V_{Bi}'''VO \cdot V_{Bi}'''$ . The increase of oxygen vacancies defects would induce a new intermediate energy level between BiOCl and SiC through Bi-C bonds [9,36]. On the other hand, the larger surface area and more active sites brought by the special feathery-like morphology was favorable for beneficial harvest of visible light which can be proven by the SEM image and BET results. Obviously, the injection of SiC with different type could modified the photo-adsorption properties of the composites by adjusting the band structure and morphology.

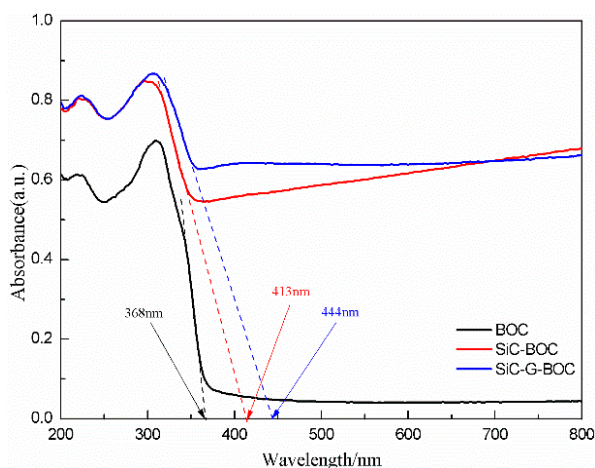
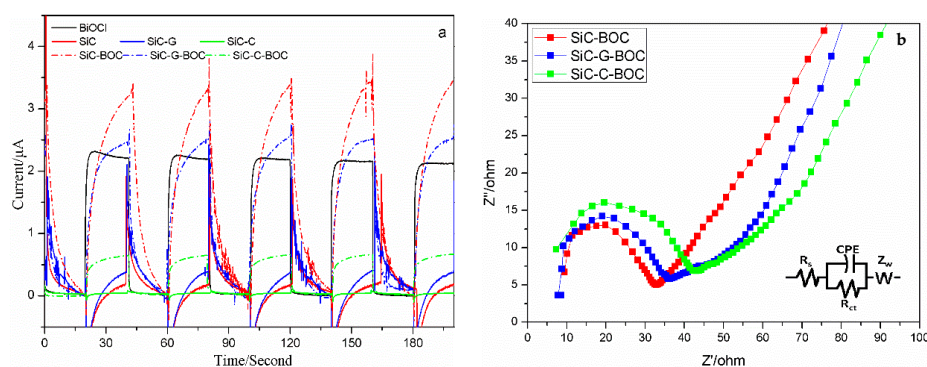


Figure 8. UV-Vis absorption spectra of BiOCl, SiC-BOC and SiC-G-BOC.

Photoelectrochemical measurement were carried out to analyze the photo-induced charge separation and migration efficiency of as-prepared photocatalysts. The transient photocurrent responses were shown in Figure 9a. It is noticeable that the synthesis of SiC/BOC significantly enhanced the photocurrent, whose highest intensity can reach 1.5 times that of pure BOC and 20 times that of raw SiC, implying a great improvement in separation of the photoexcited electron–hole pairs for the heterostructured composites. The photocurrent of SiC-C-BOC was distinctly smaller than that of the other two composite samples, revealing the decisive role of carbon in transfer of photoelectrons. The even higher current intensity of SiC-BOC compared with SiC-G-BOC was in the view of the closer interfacial interaction and quicker transmission, owing to the coupling through Bi-C bonds and growing contact area arising from tiny grain. To further investigate the internal resistances and charge transport performance of the photocatalysts, electrochemical impedance spectroscopy (EIS) measurements was employed. The electrolyte solution resistance ( $R_s$ ) and charge transfer resistance ( $R_{ct}$ ) was obtained by the fitting with electrical equivalent circuit model in Figure 9b and listed in Table 2. The semicircle radius of Nyquist plots were intently related to the resistance of the electrodes, further reflecting the interfacial transfer process and the efficiency of charges separation. The smaller the curve radius, the lower the value of  $R_{ct}$  charge transfer resistance value, which implied a higher electron–hole pair transmission and separation efficiency. Apparently, heterojunction photocatalyst SiC-BOC showed the smallest semicircle radius and value of  $R_{ct}$ , demonstrating that the combination

of carbon-coated SiC and BOC improved the electron transport properties efficiently. The Warburg diffusion impedance ( $Z_w$ ) in equivalent circuit model, which corresponded to the linear part in Nyquist plot, was affected by the morphology of particles on working electrodes. With the angle of line to y axis increased from  $45^\circ$  to  $90^\circ$ , the morphology changed from planar to spherical. The plot more parallel to the y axis indicated that SiC-BOC presented a more curved and average geometry, consistent with the structure exhibited in SEM pictures.



**Figure 9.** (a) Photocurrent responses of the BOC, SiC and SiC/BOC samples. (b) Electrochemical impedance spectra (EIS) of BOC and SiC/BOC samples.

**Table 2.** Photocurrent intensity of BOC, SiC and SiC/BOC samples and parameters of equivalent circuits for the impedance data of SiC-BOC, SiC-G-BOC and SiC-C-BOC.

	Current/ $\mu\text{A}\cdot\text{cm}^{-2}$		Current/ $\mu\text{A}\cdot\text{cm}^{-2}$	$R_s$ ( $\Omega\cdot\text{cm}^2$ )	$R_{ct}$ ( $\Omega\cdot\text{cm}^2$ )
SiC	0.16	SiC-BOC	3.29	6.44	24.86
SiC-G	0.37	SiC-G-BOC	2.52	6.52	30.25
SiC-C	0.03	SiC-C-BOC	0.65	6.71	37.16
BiOCl	2.17		-		-

In the previous works, research on photocatalytic properties of BOC was mainly focused on pollutant degradation. However, seldom did the reports carry information about solar-to-hydrogen conversion. Here, the hydrogen production of the composites photocatalysts was evaluated as shown in Figure 10. The average  $\text{H}_2$  evolution was  $2.96$  and  $4.28 \mu\text{mol}\cdot\text{g}^{-1}\cdot\text{h}^{-1}$  for SiC-BOC and SiC-G-BOC, respectively, which is much higher than pure BiOCl ( $0.12 \mu\text{mol}\cdot\text{g}^{-1}\cdot\text{h}^{-1}$ ) [37]. After combination of SiC and BOC, the narrowed band gap resulted an enhanced visible light utilization leading to an easier excitation of photo-induced electron-hole pairs and quicker transmit route from BOC to SiC for electrons. The promoted hydrogen evolution of SiC-G-BOC compared with SiC-BOC may attributed to the optimization of SiC brought by high-temperature graphitization. However, interestingly, the quantity of  $\text{O}_2$  correspondingly enlarged with the  $\text{H}_2$  production expansion was only observed in SiC-BOC.

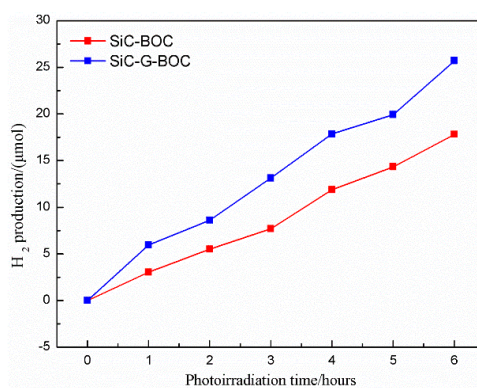


**Figure 10.** Hydrogen production of SiC and SiC/BOC samples.

The photocatalytic performances of as-prepared samples was investigated by degradation of TC-HCl in aqueous solution in Figure 11a. Apparently, both the composite samples displayed superior adsorption capacity for TC-HCl than the pure BOC due to the introduction of microporous SiC with high specific surface area and coupling between the two semiconductors. Moreover, the SiC-BOC sample exhibited an outstanding photocatalytic performance, in that TC-HCl almost completely degraded within 50 min of illumination, while the final degradation rates of BOC and SiC-G-BOC were about 75% and 70%, respectively. The kinetic study in the photodegradations of TC-HCl was employed whose degradation can be simplified each as a pseudo-first-order reaction:  $\ln(C_0/C) = kt$ . The reaction rate constants ( $k$ ) fitted from the slop of the  $\ln(C_0/C)$  versus irradiation time were shown in Figure 11b. The ( $k$ ) values of SiC-BOC reached as high as about  $0.068 \text{ min}^{-1}$ , which was about three times that of the other two samples. Even though the SiC-G-BOC samples performed a higher degradation rate, but the lower ( $k$ ) value than BOC implied that surface area was not the primary factor determining the photocatalytic efficiency of the composites. Taken together, the supreme photocatalytic performance of SiC-BOC was ascribed to the specific morphology resulted in remarkable adsorption capacity and sufficient visible light absorbance, and efficient heterojunction interface between two components through Bi-C bonds, which can provide more active sites and effective transportation, promote the harvest of visible light and restrain the recombination of photo-induced charges more effectively. The recycling tests of TC-HCl degradation upon SiC-BOC also displayed acceptable stability and recyclability in Figure 11c. The results of the trapping experiment via dissolving different scavengers in the reaction solution with SiC-BOC photocatalysts was studied in order to detect the main oxidative species in the photocatalytic process, as shown in Figure 11d. The photocatalytic degradation was not affected by the addition of IPA (a quencher of  $\cdot\text{OH}$ ). However, the inhibition with the dispersion of radicals TEOA (a quencher of  $\text{h}^+$ ) and BQ (a quencher of  $\cdot\text{O}_2^-$ ) can be obviously observed, highlighting the crucial role of  $\cdot\text{O}_2^-$  radicals in the photodegradation system. Therefore, the degradation of TC-HCl over SiC-BOC samples was dominated by  $\cdot\text{O}_2^-$  radicals, and involved by the direct hole oxidation process to an extent.

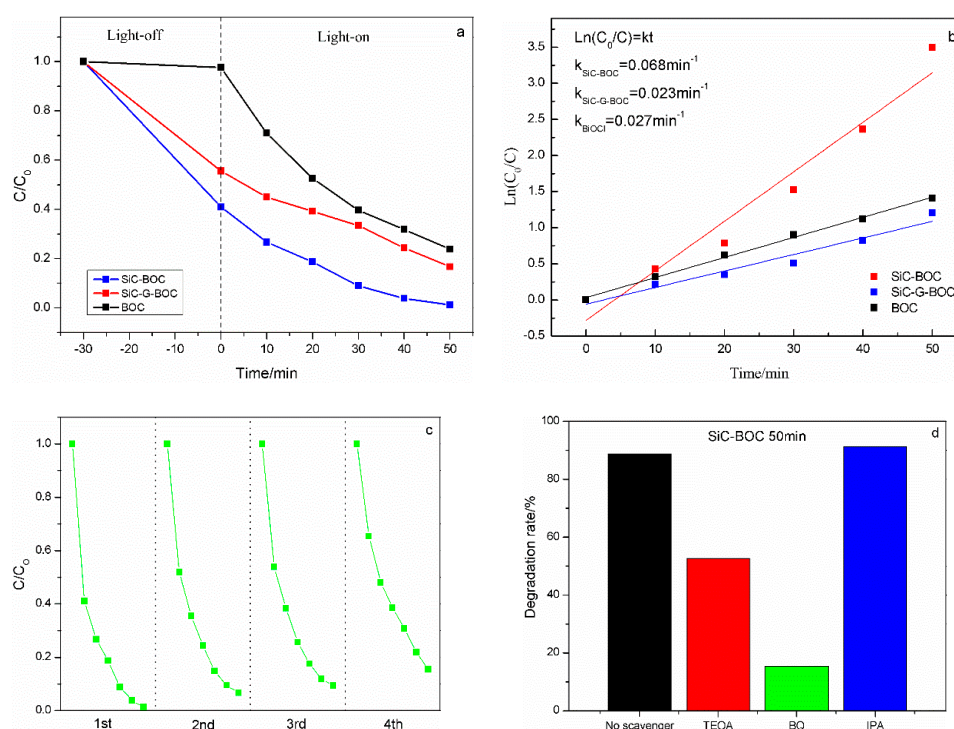


**Figure 11.** (a) Photocatalytic degradation and (b) photocatalytic kinetic curves for the degradations of TC-HCl in the presence of BOC, SiC-BOC and SiC-G-BOC. (c) Recycling tests and (d) Trapping of active species during the photodegradation of TC-HCl over SiC-BOC.

The photocatalytic results above disclosed that the formation of heterojunctions via the combination of BiOCl and SiC can enhance their activities significantly under irradiation with visible light. Based on those observations, a proposed mechanism for the photocatalytic reactions occurring on SiC-BOC composite photocatalysts was presented in Figure 12. The photocatalytic processes of the SiC/BiOCl nanosheets can be described as follows: Excited by Xe lamp irradiation, the generation, transition and recombination of photoinduced electron–hole pairs happened in both semiconductors. The excited hole on BiOCl will transfer to the surface and degrade the nearby TC-HCl directly. Due to the appropriate straddling band structure and intimately contacted interface, the irradiated electrons on BOC could inject into the CB of SiC, then captured by  $O_2$  dissolved in solution to produce superoxide radicals  $\cdot O_2^-$  which were also active in photodegradation. Owing to the special electronic property of carbon, part of photogenerated electrons can further transfer to the carbon cover of SiC and react with the pollutants. After the combination, the generation of electron–hole pairs increased because of the improved optical absorption performance as discussed in Figure 8. The transfer of photogenerated electrons was accelerated by the quick transport channel Bi-C bonds, which decreased the recombination of photogenerated electrons and holes relevantly. Additionally, on account of the enhanced adsorption capacity and chemical activity caused by carbon-coated SiC, the reaction with the pollutants was also apparently reinforced.

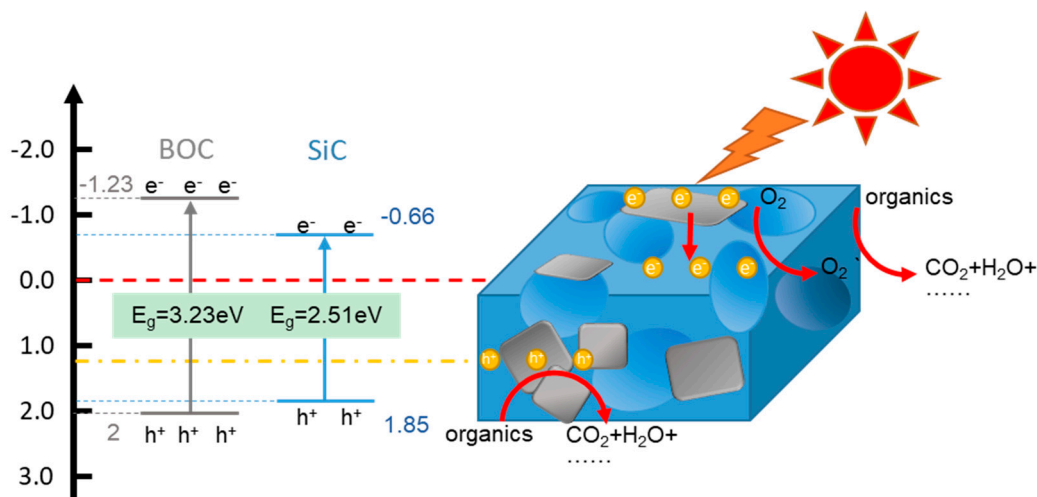


Figure 12. Proposed schematic of the SiC-BOC composite photocatalysts.

The photocatalytic activity of SiC-BOC was accomplished by the formation of heterojunctions via the combination of BiOCl and SiC. The advantage of the two semiconductors was taken by the composites. SiC, as the substrate for the nucleation and subsequent growth of BOC, benefited the light harvest in visible region for its limited band gap and multiple reflected cavity, enhanced the adsorption capacity by its microporous structure, and mediated the morphologies of BOC via the carbon cover. During the formation of the SiC-BOC hybrid, the resulted BOC nucleated and stuck on SiC, constructing the heterojunction interfaces. The Bi-C bonding only produced in SiC-BOC, further tightening the chemical coupling to promoted thermal stability and assist the carrier transmission between two semiconductors. The relation between the growth of (010) facets and photoactivities is disclosed in Table 3. With the increasing exposure of (010) facets, the growth along [001] direction was inhibited resulting a feathery-like structure composed of BOC slab with small size. As a consequence of the specific structure, charge separation was facilitated with the enlarging contact area, adsorption and reaction activity was improved by the interlaced structure, and the band gap was adjusted through growing oxygen vacancies.

**Table 3.** The relation between the exposure of (010) facets and photoactivities.

Samples	BET (m <sup>2</sup> /g)	Thickness (nm)	I(001)/I(110)	FWHM (001)	K (mol L <sup>-1</sup> s <sup>-1</sup> )	(C <sub>0</sub> - C <sub>t</sub> )/C <sub>0</sub>
SiC-BOC	197.0	70	0.43	2.83	0.068	96.9
SiC-G-BOC	177.0	100	0.46	1.95	0.023	70.0
SiC-C-BOC	11.6	250	0.49	1.22	-	-
BOC	5.3	360	8.30	-	0.027	75.5

### 3. Experimental

#### 3.1. Synthesis of SiC

SiC was prepared by an environmentally friendly synthesis combining sol-gel procedure and carbothermal reduction [38]. In a typical sol-gel procedure, P123 was dissolved in the solution consisting of 3 mL deionized water, 2.4 mL ethanol and 0.3 mL of 1 M HCl under magnetic stirring at room temperature to form a homogeneous solution. Then, Tetraethoxysilane and glucose were added in the mixture above and continuously stirred at 90 °C for 12 h. On completion of the reaction, the SiC precursor was obtained after dried at 120 °C. Subsequently, the as-prepared aerogel SiC precursor was pre-carbonized in air at 550 °C for 1.5 h, and then calcined at 1450 °C for 8 h in a flowing Ar atmosphere. After the furnace was cooled to room temperature, the cottage cheese-like SiC was obtained. In order to study the effort of carbon's form and quantity, SiC-G and SiC was also used in the synthesis of the composites. For completely removing the residual carbon in SiC, SiC-C was manufactured by heating in the air at 850 °C for 5 h. A high-temperature graphitization was performed for preparing SiC-G with procedure as follows: the as-prepared SiC was placed into a graphite crucible which was loaded into a high temperature furnace for thermally annealing. The synthesis conditions were set at pressure about 800 mbar under Ar gas and temperature about 1600 °C. Due to the loss of Si atoms and the reconstruction of the C atom, the condition of carbon on surface was changed after decomposition apparently [39].

#### 3.2. Synthesis of SiC/BOC Composites

SiC-BiOCl were synthesized by a hydrothermal method as pictured in the previous report [6]. In detail, 0.2 g SiC of different type was spread in 15 mL of distilled water followed by ultrasonic bath for 30 min for completely dispersing the agglomerated powder. Then, 1 mmol Bi(NO<sub>3</sub>)<sub>3</sub>·5H<sub>2</sub>O and 1 mmol KCl were initially dissolved in the solution at room temperature and continuously stirred for 30 min. The mixture above was shifted into a 25 mL autoclave and kept heated at 160 °C for 12 h. After cooling down to room temperature, the resulting precipitates were gathered and thoroughly washed with deionized water and ethanol, and dried at 60 °C. The obtained final product was denoted as SiC-BOC. According to this method, SiC-G-BOC, SiC-C-BOC composites and pure BOC were also synthesized as comparison, respectively.

#### 3.3. Characterization

The crystalline phase and composition of obtained products was characterized through the patterns recorded by a D8 Advance X-ray diffractometer (D8 Advance, Bruker, Billerica, MA, USA) with Cu K $\alpha$  radiation ( $\lambda = 1.54178 \text{ \AA}$ ) at 40 kV and 40 mA. The chemical states and surface properties of the samples were determined by X-ray photoelectron spectroscopy (ESCALAB 250, Thermo Fisher Scientific, Waltham, MA, USA) with a monochromatic Al K $\alpha$  as the excitation source. The optical properties of the samples were measured using a UV-Vis spectrophotometer (UV2250, Shimadzu, Kyoto, Japan), in which BaSO<sub>4</sub> was used as a reflectance standard. The surface morphologies of the as-prepared samples were observed and characterized by scanning electron microscopy (S-4800 field emission, Hitachi, Tokyo, Japan) and high-resolution transmission electron microscope (JEM 2100, JEOL, Tokyo, Japan). The thermal properties were characterized by TG analysis (SDT Q600, TA Instruments, New Castle, DE, USA) at a heating rate of 10 °C·min<sup>-1</sup> from 20 °C to 900 °C in air to investigate the

thermal stability. A Builder 4200 instrument was used to measure the Brunauer–Emmett–Teller (BET) surface areas of the samples at liquid nitrogen temperature.

### 3.4. Photoelectrochemical Measurements

Photocurrent measurements were conducted by an electrochemical workstation (CHI760, Chenhua Instrument, Shanghai, China) coupled with a Xe lamp (PLS-SXE300UV, TrustTech, Beijing, China) using a standard three-electrode configuration with 0.5 M Na<sub>2</sub>SO<sub>4</sub> as electrolyte solution. The platinum plate (1.0 × 1.0 cm) electrode, the prepared samples photoelectrode, a standard Ag–AgCl electrode were utilized as counter, working and reference electrodes, respectively.

### 3.5. Photocatalytic Activity Tests

The photocatalytic activity was evaluated by the photodegradation of TC-HCl in aqueous solution and photocatalytic H<sub>2</sub>-production. The light source of both two process was a 300 W Xe arc lamp equipment with an average light intensity of 120 mW·cm<sup>-2</sup>. The photocatalytic H<sub>2</sub>-production measurement was performed in Labsolar-6A system (Perfectlight Technology, Beijing, China), which consists of a 300-mL Pyrex glass reaction cell connected to a closed gas circulation and evacuation system. In a typical reaction, the photoreaction solution included 100 mg photocatalysts, 100 mL deionized water containing 0.1 M Na<sub>2</sub>SO<sub>3</sub> and 0.1 M Na<sub>2</sub>S as sacrificial reagents. A continuous magnetic stirring was maintained at the bottom of reactor during the entire experiment to guarantee the photocatalysts in suspension. The reaction temperature was sustained at ambient temperature by circular cooling water system during the whole photocatalytic process. The hydrogen evolved was sampled and analyzed by online thermal conductivity detector using a gas chromatograph (shiweipxGC-7806, TCD, with Ar as carrier gas, Perfectlight Technology, Beijing, China) every 1 h of illumination, which lasted for 5 h.

The photodegradation of TC-HCl in aqueous solution was carried out in a typical experiment. Briefly, 50 mg of the solid sample was added into the reactor contained 50 mL of TC-HCl aqueous solution at an initial concentration of 50 mg/L. Prior to lighting up the illuminant, the adsorption–desorption equilibrium was established by continuously magnetic stirring in the dark for 30 min. Then, 4 mL of the suspension was taken out at a 10-min interval and centrifuged to remove residual catalysts to obtain a purified liquid before the next measurement. The clarified solution was detected via a UV–vis spectrophotometer (UV2250, Shimadzu, Kyoto, Japan), at the characteristic absorption wavelength of 358 nm and further analyzed to determine its concentration after photodegradation. A cyclic experiment repeated 3 times was carried out to judge the photocatalytic stability of the samples.

### 3.6. Determination of Reactive Species

To explore the mechanism of photocatalytic degradation, the trapping experiment was conducted to probe the decisive active species what direct influence the reaction rates. The detection process was similar to the former test, except for the additional introduction of 1 mM trapping agents including TEOA, IPA, BQ to TC-HCl solution, which could quench h<sup>+</sup>, ·OH, and ·O<sup>2-</sup>, respectively. The addition of quenchers was prior to the photocatalysts. The final concentration after 50 min was evaluated to tell the result of capture and the variation of photocatalytic efficiency.

## 4. Conclusions

In the present study, an attempt to combine two semiconductors, BiOCl and SiC—one of which was only UV responsive—to fabricate heterojunction photocatalysts was presented, and successfully accomplished by simply depositing a BiOCl slab onto the surface of carbon-coated SiC. The resulting SiC-BOC composites possessed significantly enhanced photocatalytic activities owing to the improved optical absorption in visible region, high rate of carrier separation, easy transfer at the interface and promoted adsorption capacity, which can be reasonably ascribed to the well-built heterojunction structure and involvement of carbon-rich SiC in the growth of BiOCl. The best performance of the photocatalyst was achieved in SiC-BOC, whose advancement can be summarized as follows: Firstly,

due to the more negative conduction band (CB) position of BiOCl and tightly contacted interface, the migrations of electrons was accelerated through Bi-C bonds from BiOCl to SiC, which also avoided the quick recombination of electrons and holes. Secondly, with the increasing exposure of (010) facets, the specific morphologies with high surface area composed by microporous SiC and interlaced BOC nanostructure increased the number of reactive sites and advanced the absorption capacity. Finally, the forms of carbon covered on the SiC particles inhibited the growth of BiOCl along [001] orientation to different extent. The work disclosed that the formation of heterojunctions via the combination of BiOCl and SiC significantly improved photocatalytic activity and photoelectrochemical behavior of the composites. The connection of carbon with the growth of BiOCl was also revealed which provided a new idea for the adjustment to the morphology and growth of BiOCl-based composites.

**Author Contributions:** Conceptualization, W.L. and X.Y.; Formal analysis, W.L. and Q.L.; Data curation, W.L.; Writing—original draft, W.L.; Writing—review & editing, W.L.; Q.L.; X.Y.; X.C. and X.X.; Project administration, X.Y.; Funding acquisition, X.Y. and X.C.; All authors have read and agreed to the published version of the manuscript.

**Funding:** This work was supported by National Key R&D Program of China (Grant No. 2018 YFB0905701), the Key-area Research and Development Program of Guangdong Province (Grant No. 2019 B010126001), Youth Program of National Natural Science Foundation of China (Grant No. 51902182), Outstanding Youth Fund of Shandong Province (Grant No. ZR2019 JQ01), Natural Science Foundation of Shandong Province (Grant No. ZR2019 BEM011) and Fundamental Research Funds of Shandong University (Grant No. 2018 JCG01).

**Conflicts of Interest:** The authors declare no conflict of interest.

## References

1. Sirés, I.; Brillas, E. Remediation of water pollution caused by pharmaceutical residues based on electrochemical separation and degradation technologies: A review. *Environ. Int.* **2012**, *40*, 229. [[CrossRef](#)]
2. Li, J.; Yu, Y.; Zhang, L. Bismuth oxyhalide nanomaterials: Layered structures meet photocatalysis. *Nanoscale* **2014**, *6*, 8473. [[CrossRef](#)] [[PubMed](#)]
3. Zhou, C.; Lai, C.; Xu, P.; Zeng, G.; Huang, D.; Zhang, C.; Cheng, M.; Hu, L.; Wan, J.; Liu, Y. In Situ Grown AgI/Bi<sub>12</sub>O<sub>17</sub>C<sub>12</sub> Heterojunction Photocatalysts for Visible Light Degradation of Sulfamethazine: Efficiency, Pathway and Mechanism. *ACS Sustain. Chem. Eng.* **2018**, *6*, 4174–4184. [[CrossRef](#)]
4. Zhang, X.; Ai, Z.; Jia, F.; Zhang, L. Generalized One-Pot Synthesis, Characterization, and Photocatalytic Activity of Hierarchical BiOX (X = Cl, Br, I) Nanoplate Microspheres. *J. Phys. Chem. C* **2008**, *112*, 747–753. [[CrossRef](#)]
5. Cheng, H.; Huang, B.; Dai, Y. Engineering BiOX (X = Cl, Br, I) nanostructures for highly efficient photocatalytic applications. *Nanoscale* **2014**, *6*, 2009. [[CrossRef](#)] [[PubMed](#)]
6. Jing, J.; Zhao, K.; Xiao, X.; Zhang, L. Synthesis and Facet-Dependent Photoreactivity of BiOCl Single-Crystalline Nanosheets. *J. Am. Chem. Soc.* **2012**, *134*, 4473–4476. [[CrossRef](#)]
7. Ye, L.; Zan, L.; Tian, L.; Peng, T.; Zhang, J. The {001} facets-dependent high photoactivity of BiOCl nanosheets. *Chem. Commun.* **2011**, *47*, 6951–6953. [[CrossRef](#)] [[PubMed](#)]
8. Yu, J.; Bo, W.; Lin, Z.; Hong, G.; Sun, W.; Xu, L. Flowerlike C-doped BiOCl nanostructures: Facile wet chemical fabrication and enhanced UV photocatalytic properties. *Appl. Surf. Sci.* **2013**, *284*, 497–502. [[CrossRef](#)]
9. Guan, M.; Xiao, C.; Zhang, J.; Fan, S.; An, R.; Cheng, Q.; Xie, J.; Zhou, M.; Ye, B.; Xie, Y. Vacancy Associates Promoting Solar-Driven Photocatalytic Activity of Ultrathin Bismuth Oxychloride Nanosheets. *J. Am. Chem. Soc.* **2013**, *135*, 10411–10417. [[CrossRef](#)]
10. Li, Z.; Qu, Y.; Hu, K.; Humayun, M.; Chen, S.; Jing, L. Improved photoelectrocatalytic activities of BiOCl with high stability for water oxidation and MO degradation by coupling RGO and modifying phosphate groups to prolong carrier lifetime. *Appl. Catal. B Environ.* **2017**, *203*, 355–362. [[CrossRef](#)]
11. Jiang, J.; Zhang, L.; Li, H.; He, W.; Yin, J.J. Self-doping and surface plasmon modification induced visible light photocatalysis of BiOCl. *Nanoscale* **2013**, *5*, 10573. [[CrossRef](#)]
12. Kong, L.; Jiang, Z.; Lai, H.C.; Xiao, T.; Edwards, P.P. Does noble metal modification improve the photocatalytic activity of BiOCl? *Prog. Nat. Sci.* **2013**, *23*, 286–293. [[CrossRef](#)]
13. Li, Q.; Zhao, X.; Yang, J.; Jia, C.J.; Jin, Z.; Fan, W. Exploring the effects of nanocrystal facet orientations in g-C<sub>3</sub>N<sub>4</sub>/BiOCl heterostructures on photocatalytic performance. *Nanoscale* **2015**, *7*, 18971–18983. [[CrossRef](#)]

14. Ye, L.; Su, Y.; Jin, X.; Xie, H.; Zhang, C. Recent advances in BiOX (X = Cl, Br and I) photocatalysts: Synthesis, modification, facet effects and mechanisms. *Environ. Sci. Nano* **2014**, *1*, 90–112. [[CrossRef](#)]
15. Steenackers, M.; Sharp, I.D.; Larsson, K.; Hutter, N.A.; Stutzmann, M.; Jordan, R. Structured Polymer Brushes on Silicon Carbide. *Chem. Mater.* **2010**, *22*, 272–278. [[CrossRef](#)]
16. Li, X.; Zhou, X.; Gao, Q.; Yuan, J.; Wen, J.; Fang, Y.; Liu, W.; Zhang, S.; Liu, Y. Metal-free carbon nanotube—SiC nanowire heterostructures with enhanced photocatalytic H<sub>2</sub> evolution under visible light irradiation. *Catal. Sci. Technol.* **2015**, *5*, 2798–2806.
17. Zhu, K.; Guo, L.; Lin, J.; Hao, W.; Shang, J.; Jia, Y.; Chen, L.; Jin, S.; Wang, W.; Chen, X. Graphene covered SiC powder as advanced photocatalytic material. *Appl. Phys. Lett.* **2012**, *100*, 197. [[CrossRef](#)]
18. Lu, W.; Guo, L.; Jia, Y.; Guo, Y.; Li, Z.; Lin, J.; Huang, J.; Wang, W. Significant enhancement in photocatalytic activity of high quality SiC/graphene core-shell heterojunction with optimal structural parameters. *RSC Adv.* **2014**, *4*, 46771–46779. [[CrossRef](#)]
19. Zhang, L.; Niu, C.G.; Xie, G.X.; Wen, X.J.; Zhang, X.G.; Zeng, G.M. Controlled Growth of BiOCl with Large {010} Facets for Dye Self-Photosensitization Photocatalytic Fuel Cells Application. *ACS Sustain. Chem. Eng.* **2017**, *5*, 4619–4629. [[CrossRef](#)]
20. Zhao, Y.; Tan, X.; Yu, T.; Wang, S. SDS-assisted solvothermal synthesis of BiOBr microspheres with highly visible-light photocatalytic activity. *Mater. Lett.* **2016**, *164*, 243–247. [[CrossRef](#)]
21. Fang, W.Q.; Zhou, J.Z.; Liu, J.; Chen, Z.G.; Yang, C.; Sun, C.H.; Qian, P.G.R.; Zou, P.J.; Qiao, P.S.Z.; Yang, P.H.G. Hierarchical Structures of Single-Crystalline Anatase TiO<sub>2</sub> Nanosheets Dominated by {001} Facets. *Chem. A Eur. J.* **2011**, *17*, 1423–1427. [[CrossRef](#)] [[PubMed](#)]
22. Oh, Y.S.; Cho, W.S.; Kim, C.S.; Lim, D.S.; Cheong, D.S. XPS Investigation of Si<sub>3</sub>N<sub>4</sub>/SiC Nanocomposites Prepared Using a Commercial Polymer. *J. Am. Ceram. Soc.* **1999**, *82*, 1076–1078. [[CrossRef](#)]
23. Akhavan, O.; Abdollahad, M.; Esfandiari, A.; Mohatashamifar, M. Photodegradation of Graphene Oxide Sheets by TiO<sub>2</sub> Nanoparticles after a Photocatalytic Reduction. *J. Phys. Chem C* **2010**, *114*, 12955–12959. [[CrossRef](#)]
24. Gao, F.; Zeng, D.; Huang, Q.; Tian, S.; Xie, C. Chemically bonded graphene/BiOCl nanocomposites as high-performance photocatalysts. *Phys. Chem. Chem. Phys.* **2012**, *14*, 10572. [[CrossRef](#)]
25. Xu, L.; Yan, P.; Li, H.; Ling, S.; Xia, J.; Qiu, J.; Xu, Q.; Li, H.; Yuan, S. Metallic Bi self-doping BiOCl composites: Synthesis and enhanced photoelectrochemical performance. *Mater. Lett.* **2017**, *196*, 225–229. [[CrossRef](#)]
26. Akhavan, O.; Ghaderi, E. Photocatalytic Reduction of Graphene Oxide Nanosheets on TiO<sub>2</sub> Thin Film for Photoinactivation of Bacteria in Solar Light Irradiation. *J. Phys. Chem. C* **2009**, *113*, 20214–20220. [[CrossRef](#)]
27. Song, Z.; Dong, X.; Wang, N.; Zhu, L.; Luo, Z.; Fang, J.; Xiong, C. Efficient photocatalytic defluorination of perfluorooctanoic acid over BiOCl nanosheets via a hole direct oxidation mechanism. *Chem. Eng. J.* **2017**, *317*, 925–934. [[CrossRef](#)]
28. Zhuo, Q.; Deng, S.; Yang, B.; Huang, J.; Yu, G. Efficient Electrochemical Oxidation of Perfluorooctanoate Using a Ti/SnO<sub>2</sub>-Sb-Bi Anode. *Environ. Sci. Technol.* **2011**, *45*, 2973–2979. [[CrossRef](#)]
29. Wang, Y.; Li, S.; Xing, X.; Huang, F.; Shen, Y.; Xie, A.; Wang, X.; Zhang, J. Self-Assembled 3D Flowerlike Hierarchical Fe<sub>3</sub>O<sub>4</sub>@Bi<sub>2</sub>O<sub>3</sub> Core-Shell Architectures and Their Enhanced Photocatalytic Activity under Visible Light. *Chem. A Eur. J.* **2011**, *17*, 4802–4808. [[CrossRef](#)]
30. Zhu, L.P.; Liao, G.H.; Bing, N.C.; Wang, L.L.; Yang, Y.; Xie, H.Y. Self-assembled 3D BiOCl hierarchitectures: Tunable synthesis and characterization. *CrystEngComm* **2010**, *12*, 3791–3796. [[CrossRef](#)]
31. Mi, Y.; Wen, L.; Wang, Z.; Cao, D.; Fang, Y.; Lei, Y. Building of anti-restack 3D BiOCl hierarchitectures by ultrathin nanosheets towards enhanced photocatalytic activity. *Appl. Catal. B Environ.* **2015**, *176–177*, 331–337. [[CrossRef](#)]
32. Wen, Z.W.; Poudel, B.; Ma, Y.; Ren, Z.F. Shape control of single crystalline bismuth nanostructures. *J. Phys. Chem. B* **2006**, *110*, 25702–25706.
33. Zhou, X.; Gao, Q.; Li, X.; Liu, Y.; Zhang, S.; Fang, Y.; Li, J. Ultra-thin SiC Layers Covered Graphene Nanosheets as Advanced Photocatalysts for Hydrogen Evolution. *J. Mater. Chem. A* **2015**, *3*, 10999–11005. [[CrossRef](#)]
34. Gnayem, H.; Sasson, Y. Nanostructured 3D Sunflower-Like Bismuth Doped BiOCl<sub>x</sub>Br<sub>1-x</sub> Solid-Solutions with Enhanced Visible Light Photocatalytic Activity as a Remarkably Efficient Technology for Water Purification. *J. Phys. Chem. C* **2015**, 841553112.
35. Sing, K.S.W. Reporting physisorption data for gas/solid systems with special reference to the determination of surface area and porosity (Recommendations 1984). *Pure Appl. Chem.* **1985**, *57*, 603–619. [[CrossRef](#)]

36. Pan, J.; Liu, G.; Qing, G.; Lu, M. On the True Photoreactivity Order of {001}, {010}, and {101} Facets of Anatase TiO<sub>2</sub> Crystals. *Angew. Chem. Int. Ed.* **2011**, *50*, 2133–2137. [[CrossRef](#)]
37. Ye, L.; Jin, X.; Leng, Y.; Su, Y.; Xie, H.; Liu, C. Synthesis of black ultrathin BiOCl nanosheets for efficient photocatalytic H<sub>2</sub> production under visible light irradiation. *J. Power Sources* **2015**, *293*, 409–415. [[CrossRef](#)]
38. Wang, Y.; Zhang, L.; Zhang, X.; Zhang, Z.; Tong, Y.; Li, F.; Wu, J.C.-S.; Wang, X. Openmouthed β-SiC hollow-sphere with highly photocatalytic activity for reduction of CO<sub>2</sub> with H<sub>2</sub>O. *Appl. Catal. B Environ.* **2017**, *206*, 158–167. [[CrossRef](#)]
39. Lu, W.; Wang, D.; Guo, L.; Jia, Y.; Ye, M.; Huang, J.; Li, Z.; Peng, Y.; Yuan, W.; Chen, X. Bipolar Carrier Transfer Channels in Epitaxial Graphene/SiC Core-Shell Heterojunction for Efficient Photocatalytic Hydrogen Evolution. *Adv. Mater.* **2015**, *27*, 7986–7991. [[CrossRef](#)]



© 2020 by the authors. Licensee MDPI, Basel, Switzerland. This article is an open access article distributed under the terms and conditions of the Creative Commons Attribution (CC BY) license (<http://creativecommons.org/licenses/by/4.0/>).